Journal of Environmental Sciences 26 (2014) 962–969

Available online at www.sciencedirect.com

Journal of Environmental Sciences

www.jesc.ac.cn

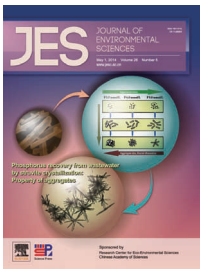

Synthesis of carbon-coated magnetic nanocomposite (Fe_3O_4@C) and its application for sulfonamide antibiotics removal from water

Xiaolei Bao[1,2], Zhimin Qiang[1,*], Jih-Hsing Chang[3], Weiwei Ben[1], Jiuhui Qu[1]

1. State Key Laboratory of Environmental Aquatic Chemistry, Research Center for Eco-Environmental Sciences, Chinese Academy of Sciences, Beijing 100085, China. E-mail: bxl5@163.com

2. State Environmental Protection Engineering Center for Pharmacy Wastewater Pollution Control, Hebei Provincial Environmental Scientific Research, Hebei 050056, China

3. Department of Environmental Engineering and Management, Chaoyang University of Technology, Wufong 41349, Taiwan, Chinese Taipei

ARTICLE INFO

Article history:
Received 17 May 2013
revised 18 October 2013
accepted 19 October 2013

Keywords:
magnetic nanocomposite
carbon shell
sulfonamides
adsorption
water

DOI: 10.1016/S1001-0742(13)60485-4

ABSTRACT

The occurrence of antibiotics in the environment has recently raised serious concerns regarding their potential threat to human health and aquatic ecosystem. A new magnetic nanocomposite, Fe_3O_4@C (Fe_3O_4 coated with carbon), was synthesized, characterized, and then applied to remove five commonly-used sulfonamides (SAs) from water. Due to its combinational merits of the outer functionalized carbon shell and the inner magnetite core, Fe_3O_4@C exhibited a high adsorption affinity for selected SAs and a fast magnetic separability. The adsorption kinetics of SAs on Fe_3O_4@C could be expressed by the pseudo second-order model. The adsorption isotherms were fitted well with the Dual-mode model, revealing that the adsorption process consisted of an initial partitioning stage and a subsequent hole-filling stage. Solution pH exerted a strong impact on the adsorption process with the maximum removal efficiencies (74% to 96%) obtained at pH 4.8 for all selected SAs. Electrostatic force and hydrogen bonding were two major driving forces for adsorption, and electron-donor-acceptor interactions may also make a certain contribution. Because the synthesized Fe_3O_4@C showed comprehensive advantages of high adsorptivity, fast magnetic separability, and prominent reusability, it has potential applications in water treatment.

Introduction

As a class of important synthetic sulfanilamide derivatives, sulfonamides (SAs) are widely used for treatment of bacterial, protozoal and fungal infections in human therapy, livestock production, and aquaculture. In China, the total consumption of antibiotics reached over 120,000 tons in 2009 (Guo, 2009). Residual antibiotics discharged from municipal wastewater treatment plants and confined animal feeding operations have been detected worldwide in surface, ground, and even drinking waters (Boxall et al., 2003; Nikolaou et al., 2007; Schwab et al., 2005). Long-term exposure to low levels of antibiotics may induce chronic allergic reactions, toxic effects and potential development of antibiotic-resistant bacteria (Boxall et al., 2003), so the occurrence of antibiotics in aquatic environments has raised an increasing concern in recent years. Consequently, there is an urgent need to develop efficient and cost-effective technologies for the removal of antibiotics from water.

A number of oxidation technologies utilizing potassium permanganate, ozone, Fenton's reagent, and chlorine have been attempted to decompose antibiotics in water (Ben et al., 2009; Chamberlain and Adams, 2006; Hu et al., 2010; Gómez-Pacheco et al., 2011; Nasuhoglu et al., 2012). Comparatively, adsorption is a conventional but effective technology for water treatment due to its relatively low

* Corresponding author. E-mail: qiangz@rcees.ac.cn

cost, easy application, and no production of harmful by-products. Some adsorbents, such as activated carbon, carbon nanotubes and sludge-derived materials, have been used to remove antibiotics from water (Choi et al., 2008; Ji et al., 2009; Ocampo-Pérez et al., 2012); however, new adsorbents, which have a high adsorption capacity and can be rapidly separated and easily regenerated, are still needed.

Functionalized magnetic nanocomposites have distinct advantages over conventional adsorbents because of their selective adsorptivity, strong magnetic responsiveness, favourable water dispersibility, and benign biocompatibility. Magnetic nanocomposites have been applied in many fields including magnetic resonance imaging, bioscience, analytical chemistry, and pollutants removal (Arsalani et al., 2010; Erathodiyil and Ying, 2011; Guo et al., 2009; Zhang et al., 2010). Carbon-coated magnetic nanocomposite, Fe_3O_4@C, has a special structure with functionalized carbon as an outer shell and magnetite as an inner core. The polysaccharide surface layer contains abundant functional sites, such as carboxylic, formyl and hydroxyl groups; moreover, this dense outer layer can protect well the inner Fe_3O_4 microspheres from being dissolved in acidic solutions (Wang et al., 2010). Previous studies about Fe_3O_4@C nanocomposite focused on its synthetic methods (Wang et al., 2006), while few have addressed its application in water treatment.

The present study aimed to investigate the adsorptive removal of five representative SAs from water using Fe_3O_4@C. Regular-shaped Fe_3O_4@C nanocomposite was synthesized in laboratory and comprehensively characterized. Thereafter, the adsorption kinetics of SAs on Fe_3O_4@C was determined through batch experiments, and the impact factors including the initial concentration of SAs, temperature and solution pH were examined in detail. Based on the surface properties of the synthesized Fe_3O_4@C and the functional groups of the studied SAs, possible adsorption mechanisms were proposed.

1 Materials and methods

1.1 Chemicals

Five commonly-used SAs, including sulfathiazole (STZ, > 98%), sulfamethoxazole (SMX), sulfamethizole (SML) and sulfadimethoxine (SDM, > 99%) were purchased from Sigma-Aldrich (St. Louis, MO, USA), and sulfamethazine (SMN) from Acros (Fair Lawn, NJ, USA). The chemical structures and major physicochemical properties of the selected SAs are provided in **Table S1** (Supporting materials). The stock solution of each SA was prepared individually at a concentration of 100 mg/L in ultrapure water, which was produced by a Milli-Q system (Advantage A10, Millipore, Billerica, MA) with a resistivity of at least 18.2 MΩ·cm. The organic solvents, methanol and acetonitrile, were of high performance liquid chromatography grade. Other chemicals were purchased from Beijing Chemical Reagents Company (Beijing, China) with at least analytical grade.

1.2 Preparation of Fe_3O_4@C

Fe_3O_4 nanoparticles (NPs) were prepared according to a sonochemical method with minor modification (Bang and Suslick, 2007). In brief, $FeCl_2{\cdot}4H_2O$ and $FeCl_3{\cdot}6H_2O$ were dissolved in pre-degassed ultrapure water with a molar ratio of Fe^{2+} to Fe^{3+} controlled at 1:2. NaOH solution (1.5 mol/L) was degassed for 15 min and then added dropwise to the above solution in nitrogen atmosphere under vigorous mechanical agitation (ca. 500 r/min) and ultrasonication conditions. The glass flask containing the reaction solution was heated at 30°C for 1 hr. The resulting Fe_3O_4 NPs were separated by an external magnetic field (2300 G), repeatedly rinsed with ultrapure water till the solution pH was close to neutral, and then dried overnight at 60°C.

Afterwards, Fe_3O_4@C nanocomposite was prepared by a hydrothermal method with certain modification (Wang et al., 2006). Oleyl amine (1 mL) was added into an aqueous suspension of Fe_3O_4 NPs (50 mL, 10 g/L) at 80°C under vigorous mechanical agitation conditions, and the reaction was allowed to proceed for 1 hr. The resulting oleic acid-stabilized Fe_3O_4 NPs were separated magnetically, and further suspended in 200 mL ultrapure water. Glucose (20 g) was dissolved in this aqueous suspension by mechanical agitation assisted with ultrasonication for 30 min. The mixture was transferred to a stainless steel autoclave (200 mL, with Teflon lining) and heated at 155°C for 3 hr. The solid product was magnetically separated, repeatedly rinsed with an ethanol solution (95%, *V/V*) for 5 times, and then dried overnight at 65°C.

1.3 Characterization of Fe_3O_4@C

Powder X-ray diffraction (XRD) patterns of Fe_3O_4 and Fe_3O_4@C NPs were analyzed on a Bruker D8 Advance X-diffractometer using Cu K_α radiation (λ = 0.15406 nm). Surface element valences, morphology, and surface properties (i.e., specific surface area, pore volume, and pore size) were determined with X-ray photoelectron spectroscopy (XPS, Escalab 250, Thermo Fisher Scientific), scanning electron microscopy (SEM, S-3000N, Hitachi), transmission electron microscopy (TEM, H-7500, Hitachi), and a surface area analyzer (ASAP2000, Micromeritics), respectively. Hysteresis loops of Fe_3O_4 and Fe_3O_4@C NPs were measured with a vibrating specimen magnetometer (VSM, BHV-50HTI, Riken Keiki) at 300 K. The pH_{pzc} of Fe_3O_4@C was determined by the mass titration method (Babić et al., 2009). The surface functional groups of Fe_3O_4@C were examined by Fourier transform infrared spectroscopy (FT-IR, Tensor 27, Bruk-

er).

1.4 Adsorption experiments

To determine the adsorption kinetics of SAs on Fe_3O_4@C, batch experiments were performed in a series of 150 mL glass conical flasks. Each flask was added with 50 mg of Fe_3O_4@C powder and 50 mL of an aqueous SA solution at an initial concentration of 100 μg/L. The solution pH was not controlled, which changed by less than 0.2 units after adsorption. The flasks were shaken in an oscillator (HZ-9610K, Taicang City, China) at 125 r/min and 25 ± 1°C. At preselected time intervals, some flasks were taken out and Fe_3O_4@C NPs were magnetically removed. After filtering the supernatant through 0.22-μm PES syringe filters (Pall, USA), the residual SA concentration was determined. Our preliminary experiment (adsorbent free) had shown that the loss of SA due to flask wall adsorption and filter interception was negligible under the experimental conditions applied. The adsorption isotherms were studied at 15, 25 and 35°C for 24 hr with the initial SA concentrations ranging from 20 to 2000 μg/L.

The effect of solution pH was examined at 25°C with 1.0 g/L dosage of Fe_3O_4@C. The pH of the working solutions, buffered with sodium borate (10 mmol/L), was adjusted from 2.3 to 10.6 with HCl or NaOH solution.

After adsorption, the Fe_3O_4@C nanocomposite was regenerated by a methanol solution (60%, *V/V*). The suspension containing the used Fe_3O_4@C and methanol solution were shaken (125 r/min) at ambient temperature for 30 min. The Fe_3O_4@C was separated magnetically, dried in oven at 65°C for 1 hr, and then reused for SA adsorption. The reusability test was performed for nine cycles in total.

1.5 Analysis of SAs

The concentrations of selected SAs were measured by ultra-performance liquid chromatography-tandem mass spectrometry (UPLC-MS/MS, Waters, Milford, MA, USA) coupled with a Symmetry C18 column (150 mm × 2.1 mm, 5-μm particle size, Waters). Formic acid (0.2%, *V/V*) and acetonitrile were used as mobile phases A and B, respectively, with a total flow rate of 0.2 mL/min at 30°C. STZ, SMN, SML, SMX and SDM were individually analyzed under an isocratic elution condition of 90:10, 85:15, 75:25, 70:25 and 60:40 (A:B), respectively. Both mobile phases were filtered through 0.22-μm membrane and then degassed ultrasonically for 10 min before use. The mass spectrometer was operated under the positive electrospray ionization (ESI+) mode and the selected ion recording (SIR) mode was adopted for quantitative analysis. Other MS parameters followed our previous work (Ben et al., 2008). Data analysis was performed with MassLynx 4.0 software (Waters).

2 Results and discussion

2.1 Characterization of Fe_3O_4@C

The XRD pattern of Fe_3O_4 NPs (**Fig. 1**) matched well with the standard magnetite crystal structure data (Joint Committee for Power Diffraction Studies, Card No. 19-0629). For the Fe_3O_4@C nanocomposite, a broad peak at $2\theta = 22°$ emerged besides the iron oxide (Fe_3O_4 or α-Fe_2O_3) diffraction peaks, which was attributed to the characteristic reflection of carbon. It indicates that the iron valence states were almost unchanged after being coated with amorphous carbon through the hydrothermal process.

The composition of Fe_3O_4@C and the valence states of its component elements were analyzed by XPS. **Figure 2a** shows that the peaks of $Fe2p_{3/2}$ and $Fe2p_{1/2}$ were located at 711.10 and 724.15 eV, respectively, in accordance with those of Fe_3O_4 (Yamashita and Hayes, 2008). The absence of the satellite peak of $Fe2p_{3/2}$ (**Fig. 2a**) further confirms that the iron oxide diffraction peaks in the XRD pattern of Fe_3O_4@C (**Fig. 1**) originated from Fe_3O_4, but not from α-Fe_2O_3. The statistical analysis of the survey line of Fe_3O_4@C (**Fig. 2b**) reveals that the atomic ratio of Fe to C was about 67:1.

The SEM image (**Fig. 3a**) shows that the synthesized Fe_3O_4@C nanocomposite had a regular shape of nanosized microspheres with a relatively narrow distribution of particle sizes (50−150 nm). The TEM image (**Fig. 3b**) shows that the aggregated Fe_3O_4 NPs were uniformly coated with a carbon shell of 20−30 nm thickness. These aggregates could be easily separated by short-time ultrasonication after being dosed into an aqueous solution.

The major structural properties of Fe_3O_4 and Fe_3O_4@C were determined by N_2 adsorption-desorption isotherms (**Table S2**). As compared to Fe_3O_4, the specific surface area and pore volume of Fe_3O_4@C decreased from 64.7 to 43.8 m^2/g and from 0.31 to 0.22 cm^3/g, respectively; but

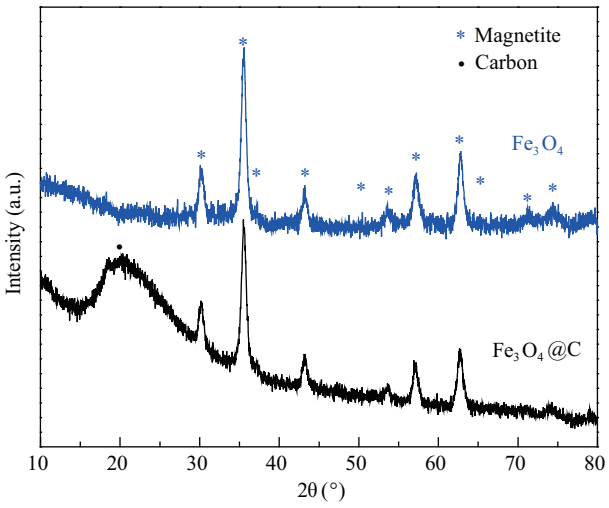

Fig. 1 XRD patterns of the synthesized Fe_3O_4 and Fe_3O_4@C.

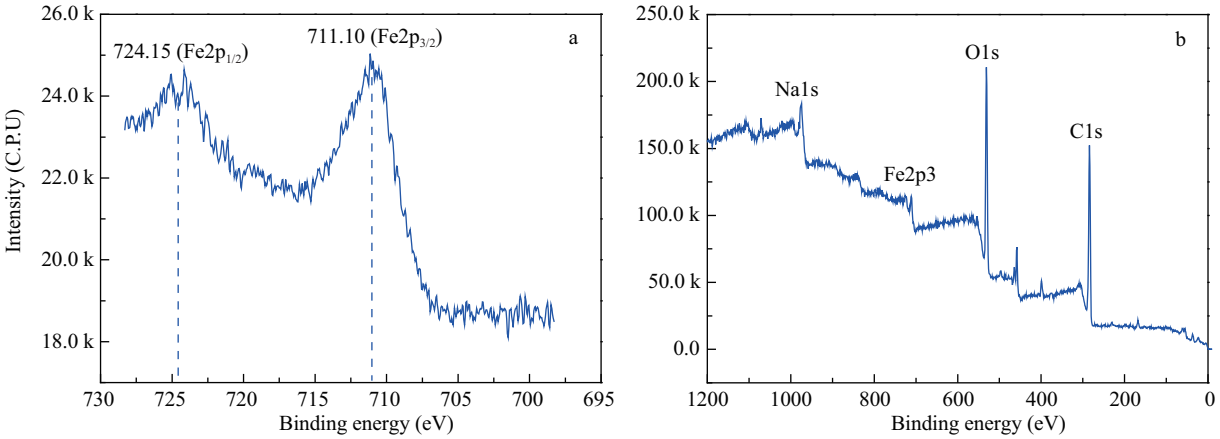

Fig. 2 XPS spectra of Fe_3O_4@C. (a) Fe 2p, and (b) the survey line.

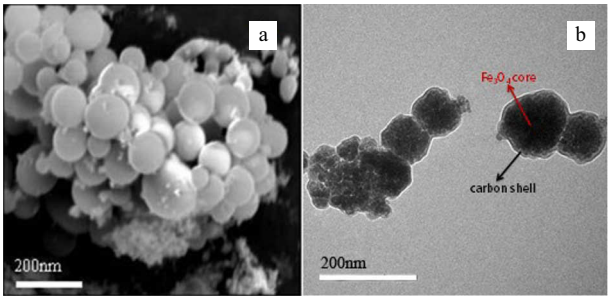

Fig. 3 Images of Fe_3O_4@C. (a) SEM, and (b) TEM.

the average pore diameter increased from 95.1 to 173.1 Å. The increased pore diameter of Fe_3O_4@C might somewhat facilitate SAs to penetrate into the inner pores of carbon shell.

The magnetic property of Fe_3O_4@C governs its separability from the working solution. **Figure 4a** shows the hysteresis loops of Fe_3O_4 and Fe_3O_4@C at 300 K. The low remanence (0.708 emu/g) of Fe_3O_4@C denoted its nearly superparamagnetic property. The saturation magnetization of Fe_3O_4@C decreased obviously to 21.7 emu/g as compared to that of Fe_3O_4 (i.e., 65.6 emu/g), which indirectly reflects the uniform and dense coating of a carbon shell. To examine the magnetic separability of Fe_3O_4@C, a magnet (2300 G) was placed near a glass bottle containing an aqueous suspension of Fe_3O_4@C NPs. It was observed that the Fe_3O_4@C NPs were quickly attracted towards the magnet and thus the original grey suspension became clear within 3 min. After removing the magnet, the Fe_3O_4@C NPs could be readily re-dispersed in water by gently shaking the glass bottle (**Fig. 4b**). Although coating a carbon shell decreased notably the saturation magnetization of Fe_3O_4@C, the remaining magnetism was still sufficient to achieve a fast separation of these particles from water.

2.2 Adsorption kinetics

Figure 5 shows that the adsorption of selected SAs onto Fe_3O_4@C was fast in the first 6 hr and became slow afterwards. The adsorption equilibrium was nearly reached at 24 hr, when the removal efficiencies of the five SAs ranged from 75% (SML) to 94% (STZ). The fast initial adsorption rate was attributed to the abundant active sites available on the Fe_3O_4@C surface; once these sites were mostly occupied, the adsorption rate decreased (Weng et al., 2009).

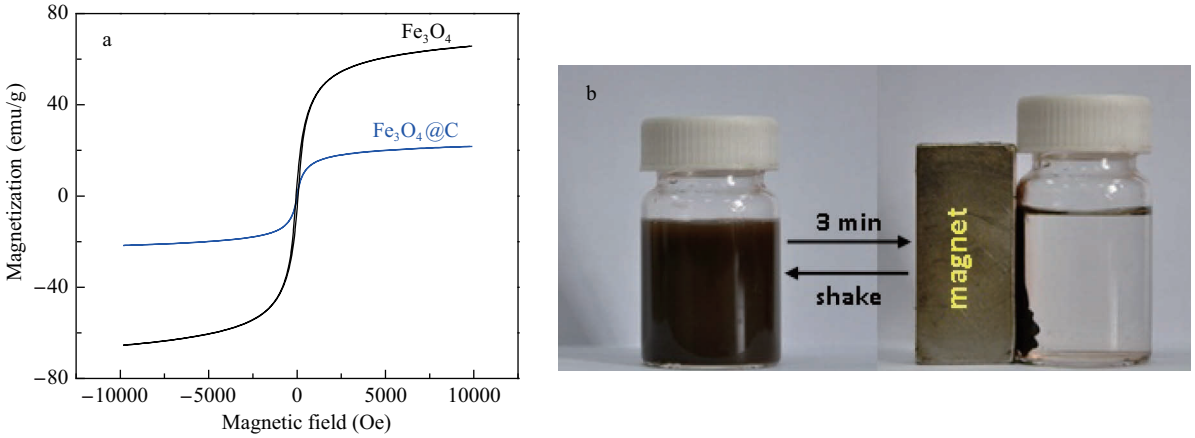

Fig. 4 (a) Magnetization curves of Fe_3O_4 and Fe_3O_4@C, and (b) illustration of the magnetic separability of Fe_3O_4@C.

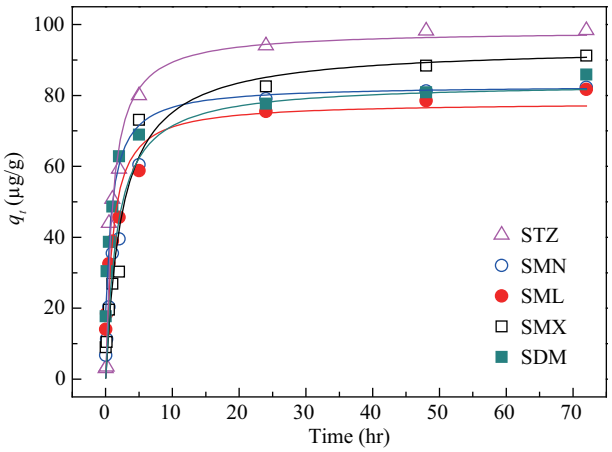

Fig. 5 Adsorption kinetics of SAs on Fe_3O_4@C. Experimental conditions: temperature = 25 ± 1°C; pH = 6.7 ± 0.2; $C_{o,SA}$ = 100 μg/L; Fe_3O_4@C dosage = 1.0 g/L. Curves represent the pseudo second-order model fitting; the standard deviations of all data points are below 5% (n = 3).

The kinetic data of SAs adsorption on Fe_3O_4@C could be expressed by the pseudo second order model (Liu et al., 2011):

$$\frac{t}{q_t} = \frac{1}{k_2 q_e^2} + \frac{1}{q_e} t \quad (1)$$

where, k_2 (g/(μg·hr)) is the adsorption rate constant; and q_t (μg/g) and q_e (μg/g) represent the adsorbed concentrations of a target SA at time t (hr) and at equilibrium, respectively.

The adsorption kinetic parameters were obtained through model simulation, as summarized in **Table S3**. The adsorption rate constants (k_2) of selected SAs ranged from 4.23×10^{-3} to 1.26×10^{-2} g/(μg·hr), and the adsorbed equilibrium concentrations (q_e) ranged from 75.9 to 97.7 μg/g.

2.3 Adsorption isotherms

The adsorption isotherms were investigated at 15, 25, and 35°C with various initial SA concentrations. Dual-mode model (DMM) (Pignatello and Xing, 1995) was adopted to fit the experimental data, which is expressed as follows:

$$q_e = k_L C_e + \frac{q_m C_e}{k_{NL} + C_e} \quad (2)$$

where, q_m (μg/g) is the maximum adsorption capacity of the non-linear part; C_e (μg/L) is the aqueous SA concentration at equilibrium; k_L (L/g) is the partition coefficient of the linear part; and k_{NL} (μg/L) is the adsorption cohesive energy coefficient.

The DMM, by combining Langmuir equation with a linear equation, considers simultaneously both the site-specific and partitioning mechanisms in the adsorption process (Zampori et al., 2009). The fitted adsorption isotherms (**Fig. 6**) show that the affinity of Fe_3O_4@C for SAs followed a decreasing order of STZ > SMX > SDM > SMN > SML. The model simulation parameters are listed in **Table S4**, with good regression coefficients (r^2 > 0.99) obtained for all selected SAs. The adsorption of SAs on Fe_3O_4@C had two stages, i.e., an initial partitioning stage and a subsequent hole-filling stage. Specifically, the SA molecules in the bulk solution were first adsorbed onto the surface of Fe_3O_4@C through linear partition; afterwards, the diffusion force continued to drive some SA molecules into the inner pores of the carbon shell of Fe_3O_4@C.

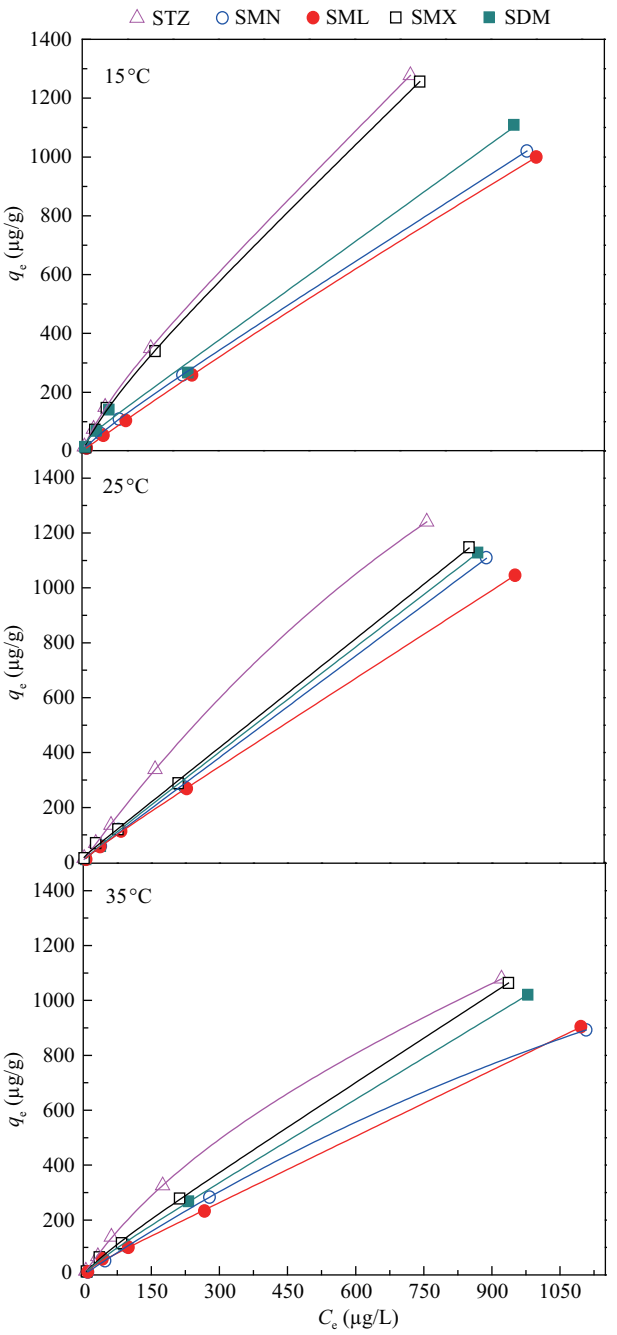

Fig. 6 Adsorption isotherms of SAs on Fe_3O_4@C fitted with Dual-mode model at different temperatures. Experimental conditions: pH = 6.7 ± 0.2; Fe_3O_4@C dosage = 1.0 g/L. The standard deviations of all data points are below 10% (n = 3).

The q_m value of each SA generally decreased with an increasing temperature, implying that the adsorption of SAs on Fe_3O_4@C was an exothermic process.

The adsorption affinity of Fe_3O_4@C was impacted significantly by the physicochemical properties of a specific SA (e.g., ionization constants, chemical structure) under a given pH condition. For example, Fe_3O_4@C exhibited the maximum affinity for STZ among the selected SAs, probably because of the minimum steric hindrance of the thiazole ring of this antibiotic. However, with respect to SDM, Fe_3O_4@C exhibited a higher affinity than expected. On the one side, the complex dimethoxypyridine moiety of SDM was likely to produce the maximum steric hindrance; on the other side, this moiety has the most lone pair electrons (six, as calculated by ChemBio3D Ultra 12.0), which could enhance the adsorption of SDM on Fe_3O_4@C through an increased electrostatic attraction force. It was also noted that Fe_3O_4@C exhibited the minimum affinity for SML, probably because of the lowest $pK_{a,2}$ value of SML (5.29, see **Table S1**). At the experimental pH (6.7 ± 0.2), SML existed predominantly as anionic form (SML^-) in water and the surface of Fe_3O_4@C was negatively charged to some extent (pH_{pzc} = 6.5). Consequently, the electrostatic repulsion force would weaken the adsorption of SML on Fe_3O_4@C. It is seen that the adsorption affinity of Fe_3O_4@C reflects a comprehensive balance among different influences induced by the physicochemical properties of a target SA.

2.4 Proposed adsorption mechanisms

The adsorption of selected SAs on Fe_3O_4@C exhibited significant pH dependence (**Fig. 7**). The results indicate that the removal efficiencies of all selected SAs reached maximum (74% to 96%) at pH 4.8, and then dropped gradually as the pH either increased to 6.0 or decreased to 2.3. Moreover, raising the pH from 6.0 to 9.0 led to a rapid drop in the removal efficiency, while a further pH increase to 10.6 had little influence on the removal efficiency of SAs.

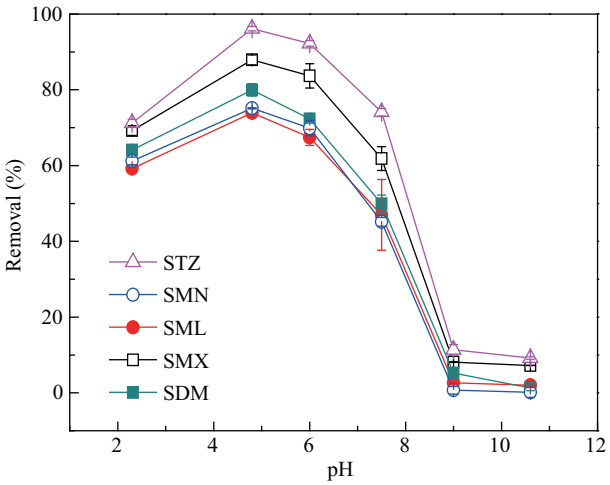

Fig. 7 Effect of pH on the adsorption of SAs on Fe_3O_4@C. Experimental conditions: temperature = 25 ± 1°C; $C_{o,SA}$ = 100 μg/L; Fe_3O_4@C dosage = 1.0 g/L; 10 mmol/L sodium borate buffer. The error bars represent the standard deviations of triplicate experiments.

The solution pH could affect both the speciation of SAs (see **Fig. S1**) and the surface charge of Fe_3O_4@C (Yang et al., 2012). The effect of pH on the removal of selected SAs can be explained by taking STZ as example, which has two ionization constants ($pK_{a,1}$ = 2.01, $pK_{a,2}$ = 7.11; **Table S1**). At pH 2.3, STZ was present as the neutral (STZ^0) and cationic (STZ^+) forms in water, and the surface of Fe_3O_4@C was positively charged (pH_{pzc} = 6.5). Thus, the electrostatic repulsion force could notably weaken the adsorption of STZ on Fe_3O_4@C. In the pH range from 4.8 to 6.0, STZ existed predominantly as the neutral form (STZ^0), thus hydrogen bonding between the N-containing groups of STZ^0 and the surface –OH of Fe_3O_4@C became the major driving force for adsorption. As the pH further increased from 6.0 to 9.0, more neutral molecules (STZ^0) were transformed to the anionic form (STZ^-); meanwhile, the surface charge of Fe_3O_4@C became more negative. Hence, the electrostatic repulsion force could impair strongly the adsorption process. At pH 10.6, only a slight decrease in the removal efficiency of STZ was observed, because a pH increase from 9.0 to 10.6 had little impact on the speciation of STZ and the surface charge of Fe_3O_4@C.

The surface functional groups of Fe_3O_4 and Fe_3O_4@C NPs were comparatively examined by FT-IR. **Figure 8** shows that both spectra had a characteristic peak at 590 cm^{-1}, denoting the presence of the Fe–O bond. Furthermore, several new peaks emerged after Fe_3O_4 was coated with a carbon shell. The peak at 3500 cm^{-1} originated from the stretching vibration of –OH (ν_{-OH}); the peaks at 2907 and 2836 cm^{-1} originated from the stretching vibration of $-CH_2$ (ν_{-CH_2}); and other peaks at 1691, 1618 and 780 cm^{-1} were probably attributed to the stretching vibration

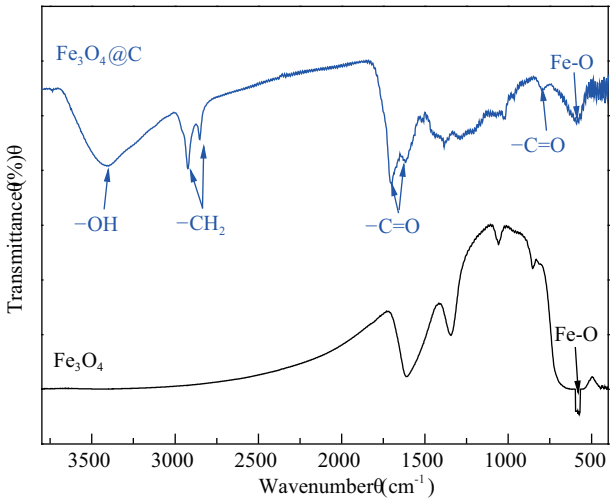

Fig. 8 FT-IR spectra of the synthesized Fe_3O_4 and Fe_3O_4@C.

of –C=O ($\nu_{-C=O}$).

The surface –OH of Fe_3O_4@C could interact with different N-containing groups of selected SAs to form three types of hydrogen bonding, as illustrated in **Scheme 1**, by taking STZ as example. Specifically, the surface –OH of Fe_3O_4@C could conjugate with the lone pair electrons of the aromatic primary amine (HB1), the secondary amine (HB2), and the thiazole-N that acts as a Lewis base (HB3), to form hydrogen bonding.

In addition, the delocalized π-bonds in the aniline group and the thiazole ring of STZ had a strong electron-withdrawing ability (Ji et al., 2010), thus could interact with the π- and σ-electrons of the surface carbonyl group of Fe_3O_4@C (–C=O, see **Fig. 8**) to form conjugate and hyper conjugate structures, respectively. These electron-donor-acceptor (EDA) interactions, including the π-π conjugation (EDA1) and σ-π hyper conjugation (EDA2) between the aniline group and the carbonyl group as well as the π-π conjugation between the thiazole ring and the carbonyl group (EDA3) (**Scheme 1**), may also promote the adsorption of selected SAs on Fe_3O_4@C.

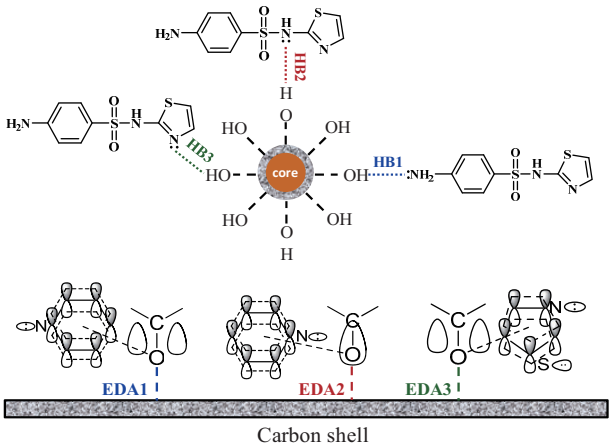

Scheme 1 Illustration of hydrogen bonding and EDA interactions between the surface functional groups (–OH, –C=O) of Fe_3O_4@C and the N-containing groups of STZ.

2.5 Reusability of Fe_3O_4@C

A methanol solution (60%, *V*/*V*) was employed to regenerate the used Fe_3O_4@C after adsorption of selected SAs. The results indicate that more than 95% of the adsorbed SAs could be readily washed off the surface of Fe_3O_4@C, and the regenerated Fe_3O_4@C showed little loss in its adsorption capacity for SAs even after nine test cycles (**Fig. S2**). Because of its effective micro-pollutants removal, fast magnetic separation, and prominent reusability, the synthesized Fe_3O_4@C has potential applications in water treatment.

3 Conclusions

In this study, a new magnetic nanocomposite (Fe_3O_4@C) was synthesized, characterized, and applied to remove five commonly-used sulfonamide antibiotics from water. Based on the experimental results, we can draw the following conclusions: (1) The synthesized Fe_3O_4@C nanocomposite had a special "core-shell" structure, with an inner core of magnetite and an evenly coated outer shell of carbon (about 20−30 nm thickness). The Fe_3O_4@C NPs were well dispersible and magnetically separable in water. (2) The adsorption kinetics of SAs on Fe_3O_4@C could be expressed by the pseudo second-order model. The adsorption isotherms, as fitted by the Dual-mode model, reveal that the adsorption process consisted of an initial partitioning stage and a subsequent hole-filling stage. (3) The solution pH exerted a strong impact on the adsorption process. The adsorption affinity of Fe_3O_4@C for an SA was primarily governed by the electrostatic force between the existing species of the SA and the surface of Fe_3O_4@C. (4) Hydrogen bonding between the N-containing groups of an SA and the surface –OH of Fe_3O_4@C played an important role in adsorption, and the electron-donor-acceptor interactions may also make a certain contribution. (5) The regenerated Fe_3O_4@C could maintain its adsorptivity well for the selected SAs.

Acknowledgments

This work was supported by the National Natural Science Foundation of China (No. 51221892), the Ministry of Science and Technology of China (No. 2012AA062606, 2012BAJ25B04), and the People Programme (Marie Curie Actions) of the European Union's Seventh Programme FP7/2007-2013 under a REA grant (No. 318926).

Supporting materials

Supplementary data associated with this article can be found in the online version.

REFERENCES

Arsalani N., Fattahi H., Nazarpoor M., 2010. Synthesis and characterization of PVP-functionalized superparamagnetic Fe_3O_4 nanoparticles as an MRI contrast agent. Expre. Poly. Lett. 4(6), 329–338.

Babić B. M., Milonjić S. K., Polovina, M. J., Kaludierović, B. V., 2009. Point of zero charge and intrinsic equilibrium constants of activated carbon cloth. Carbon 37(3), 477–481.

Bang, J. H., Suslick, K. S., 2007. Sonochemical synthesis of nanosized hollow hematite. J. Am. Chem. Soc. 129(8), 2242–2243.

Ben, W. W., Qiang, Z. M., Adams, C., Zhang, H. Q., Chen, L. P., 2008. Simultaneous determination of sulfonamides, tetracyclines and tiamulin in swine wastewater by solid-phase extraction and liquid chromatography-mass spectrometry. J. Chromatogr. A 1202(2), 173–180.

Ben, W. W., Qiang, Z. M., Pan, X., Chen, M. X., 2009. Removal of veterinary antibiotics from sequencing batch reactor (SBR) pretreated swine wastewater by Fenton's reagent. Water Res. 43(17), 4392–4402.

Boxall, A. B. A., Kolpin, D. W., Halling-Sørensen, B., Tolls, J., 2003. Are veterinary medicines causing environmental risks? Environ. Sci. Technol. 37(15), 286A–294A.

Chamberlain, E., Adams, C., 2006. Oxidation of sulfonamides, macrolides, and carbadox with free chlorine and monochloramine. Water Res. 40(13), 2517–2526.

Choi, K. J., Kim, S. G., Kim, S. H., 2008. Removal of tetracycline and sulfonamide classes of antibiotic compound by powdered activated carbon. Environ. Technol. 29(3), 333–342.

Erathodiyil, N., Ying, J. Y., 2011. Functionalization of inorganic nanoparticles for bioimaging applications. Acc. Chem. Res. 44(10), 925–935.

Gómez-Pacheco, C. V., Sánchez-Polo, M., Rivera-Utrilla, J., López-Peñalver, J., 2011. Tetracycline removal from waters by integrated technologies based on ozonation and biodegradation. Chem. Eng. J. 178(15), 115–121.

Guo, Q. Z., Mei, B., Zhou, S. X., Shi, Z. G., Feng, Y. Q., Wu, J. Y. et al., 2009. Synthesis, characterization and application of magnetic-zirconia nanocomposites. J. Non-Cryst Soli. 355(16-17), 922–925.

Guo, W., 2009. Global: The domestic, international development situation of antibiotics Southern Weekly, 2009–12-10 (H02) http://wenku.baidu. com/view/91eea7000740be1e650e9af7.html.

Hu, L. H., Martin, H. M., Strathmann, T. J., 2010. Oxidation kinetics of antibiotics during water treatment with potassium permanganate. Environ. Sci. Technol. 44(16), 6416–6422.

Ji, L. L., Chen, W., Duan, L., Zhu, D. Q., 2009. Mechanisms for strong adsorption of tetracycline to carbon nanotubes: A comparative study using activated carbon and graphite as adsorbents. Environ. Sci. Technol. 43(7), 2322–2327.

Ji, L. L., Liu, F. L., Xu, Z. Y., Zheng, S. R., Zhu, D. Q., 2010. Adsorption of pharmaceutical antibiotics on template-synthesized ordered micro-and mesoporous carbons. Environ. Sci. Technol. 44(8), 3116–3122.

Liu, W. F., Zhang, J., Zhang, C. L., Ren, L., 2011. Sorption of norfloxacin by lotus stalk-based activated carbon and iron-doped activated alumina: Mechanisms, isotherms and kinetics. Chem. Eng. J. 171(2), 431–438.

Nasuhoglu, D., Rodayan, A., Berk, D., Yargeau, V., 2012. Removal of the antibiotic levofloxacin (LEVO) in water by ozonation and TiO_2 photocatalysis. Chem. Eng. J. 189–190(1), 41–48.

Nikolaou, A., Meric, S., Fatta, D., 2007. Occurrence patterns of pharmaceuticals in water and wastewater environments. Analyt. Bioanal. Chem. 387(4), 1225–1234.

Ocampo-Pérez, R., Rivera-Utrilla, J., Gómez-Pacheco, C., Sánchez-Polo, M., López-Peñalver, J. J., 2012. Kinetic study of tetracycline adsorption on sludge-derived adsorbents in aqueous phase. Chem. Eng. J. 213, 88–96.

Pignatello, J. J., Xing, B. S., 1995. Mechanisms of slow sorption of organic chemicals to natural particles. Environ. Sci. Technol. 30(1), 1–11.

Schwab, B. W., Hayes, E. P., Fiori, J. M., Mastrocco, F. J., Roden, N. M., Cragin, D. et al., 2005. Human pharmaceuticals in US surface waters: A human health risk assessment. Regulat. Toxicol. Pharmacol. 42(3), 296–312.

Wang, H., Sun, Y. B., Chen, Q. W., Yu, Y. F., Cheng, K., 2010. Synthesis of carbon-encapsulated superparamagnetic colloidal nanoparticles with magnetic-responsive photonic crystal property. Dalton Transact. 39(40), 9565–9569.

Wang, Z. F., Guo, H. S., Yu, Y. L., He, N. Y., 2006. Synthesis and characterization of a novel magnetic carrier with its composition of Fe_3O_4/carbon using hydrothermal reaction. J. Magnet. Magnet. Mater. 302(2), 397–404.

Weng, C. H., Lin, Y. T., Tzeng, T. W., 2009. Removal of methylene blue from aqueous solution by adsorption onto pineapple leaf powder. J. Hazard. Mater. 170(1), 417–424.

Yamashita, T., Hayes, P., 2008. Analysis of XPS spectra of Fe^{2+} and Fe^{3+} ions in oxide materials. Appl. Surf. Sci. 254(8), 2441–2449.

Yang, W. B., Lu, Y. P., Zheng, F. F., Xue, X. X., Li, N., Liu, D. M., 2012. Adsorption behavior and mechanisms of norfloxacin onto porous resins and carbon nanotube. Chem. Eng. J. 179, 112–118.

Zampori, L., Stampino, P. G., Dotelli, G., 2009. Adsorption of nitrobenzene and orthochlorophenol on dimethyl ditallowyl montmorillonite: A microstructural and thermodynamic study. Appl. Clay Sci. 42(3-4), 605–610.

Zhang, S. X., Niu, H. Y., Hu, Z. J., Cai, Y. Q., Shi, Y. L., 2010. Preparation of carbon coated Fe_3O_4 nanoparticles and their application for solid-phase extraction of polycyclic aromatic hydrocarbons from environmental water samples. J. Chromatogr. A 1217(29), 4757–4764.